Inverse Problems

PURPOSE-LED PUBLISHING™

PAPER • OPEN ACCESS

Feasibility of acousto-electric tomography

To cite this article: Bjørn Jensen *et al* 2024 *Inverse Problems* **40** 075007

View the article online for updates and enhancements.

You may also like

- Sound speed uncertainty in acousto-electric tomography
Bjørn Christian Skov Jensen and Kim Knudsen
- Acousto-electric transport in MgO/ZnO-covered graphene on SiC
Y-T Liou, A Hernández-Mínguez, J Herfort et al.
- Acousto-electric tomography with total variation regularization
Bolaji James Adesokan, Bjørn Jensen, Bangti Jin et al.

This content was downloaded from IP address 158.36.4.115 on 24/04/2025 at 14:41

OPEN ACCESS
IOP Publishing
Inverse Problems

Inverse Problems **40** (2024) 075007 (18pp) https://doi.org/10.1088/1361-6420/ad4669

Feasibility of acousto-electric tomography

Bjørn Jensen[1], **Adrian Kirkeby**[2] **and Kim Knudsen**[3,*]

[1] Faculty of Information Technology, University of Jyväskylä, Jyväskylä, Finland
[2] Department of Numerical Analysis and Scientific Computing, Simula Research Laboratory, Oslo, Norway
[3] Department of Applied Mathematics and Computer Science, Technical University of Denmark, Kgs. Lyngby, Denmark

E-mail: kiknu@dtu.dk, bjorn.c.s.jensen@jyu.fi and adrian@simula.no

Received 15 August 2023; revised 8 April 2024
Accepted for publication 2 May 2024
Published 4 June 2024

Abstract

In acousto-electric tomography (AET) the goal is to reconstruct the electric conductivity in a domain from electrostatic boundary measurements of corresponding currents and voltages, while the domain is perturbed by a time-dependent acoustic wave, thus taking advantage of the acousto-electric effect. We approach the AET reconstruction in two steps: First, the interior power density is obtained from boundary measurements by solving a linear inverse and ill-posed problem; second, the interior conductivity is reconstructed from the power density by solving a non-linear and well-posed problem. Mathematically these inverse problems are fairly well understood, and reconstruction methods work well on synthetic data. This is in contrast to experimental findings. An effect can indeed be observed and data can be collected. However, the acousto-electric coupling is very weak, and consequently, the change in the measured voltage due to the acoustic perturbation might be too small compared to the background noise for viable reconstructions. In this paper, we take one step towards understanding the feasibility of AET. We provide an in-silico model of the coupled physics scenario based on standard models for the individual phenomena. Moreover, we formulate and implement numerically a full reconstruction method for the inverse problem via the two steps. We perform computational experiments with realistically chosen parameters from the context of medical imaging. The focus is on understanding the role of the acousto-electric coupling parameter and the signal-to-noise ratio (SNR). The critical signal strength is analyzed and the omnipresent Johnson–Nyquist noise is estimated.

* Author to whom any correspondence should be addressed.

Original Content from this work may be used under the terms of the Creative Commons Attribution 4.0 licence. Any further distribution of this work must maintain attribution to the author(s) and the title of the work, journal citation and DOI.

© 2024 The Author(s). Published by IOP Publishing Ltd

We obtain both positive and negative findings; we can reconstruct features even under severe noise conditions, but we also find that the SNR one is likely to face in practice is too low to obtain useful reconstructions.

Keywords: acousto-electric tomography, electrical impedance tomography, hybrid data tomography, coupled physics imaging, inverse problems, medical imaging, computational imaging

1. Introduction

In a variety of applications in imaging science, it is important to reliably image the electrical conductivity in some object or region. In medical imaging, for instance, the electric conductivity distribution in the human body carries information about the health condition of the patient, i.e. location of tumors, lung function, and brain function, and hence an image of the conductivity is very useful for medical imaging [22]. In other application domains such as Electrical Brain Stimulation, it is important to have an accurate estimate of the brain's conductivity in order to compute the interior current density generated by exterior excitation [43].

Electrical impedance tomography (EIT) is an emerging technology for non-invasive imaging that aims at reconstructing a body's electrical conductivity from measurements of current and voltages through electrodes at the surface of the body. It is considered a cheap, portable and harmless modality. It is well-known that due to the diffusive nature of electric currents, the inverse problem in EIT is highly ill-posed, thus giving rise to low-resolution images. Applications of EIT to medical imaging are diverse and include pulmonary function monitoring, early detection of breast cancer, and hemorrhagic stroke detection, see [3]. Beyond the medical domain, EIT is also used for flow monitoring and industrial testing [27, 36]. Mathematically the problem is known as the Calderón problem [11]. See also [13, 40] for more background on the mathematics and applications.

In recent years new ideas for conductivity imaging have been proposed that are often referred to as coupled physics or hybrid imaging. Broadly speaking, the idea is to utilize two separate, but coupled, physical phenomena to obtain additional information through their interaction thus making the reconstruction problem more well-posed. One such method that has been subject to extensive research interest is acousto-electric tomography (AET) [45, 46]. In AET, one perturbs the electrical conductivity of the object by acoustic waves while conducting EIT measurements. In theory, the so-called acousto-electric effect, i.e. the local change in conductivity due to change in pressure, then allows one to obtain additional internal information about the unknown conductivity, potentially leading to high-resolution images of the conductivity.

There are other hybrid imaging modalities taking advantage of the acousto-electric effect for other purposes. We highlight the promising method for the imaging of internal current flows known as ultrasound current source density imaging [41] or ultrafast acousto-electric imaging [9].

We approach the inverse problem of AET in two steps: first, we reconstruct the interior electric power density from a time series of boundary measurements of the acoustically perturbed object. Second, we reconstruct the conductivity from the power density; this is the so-called quantitative step. There is a vast literature on the mathematical and computational aspects of AET mostly focusing on the second step. The fundamental modeling originates from [5]. In [29, 30] idealistic wave modelling was considered and an inversion scheme using the spherical Radon transform was derived. The reconstruction problem was considered in [12] using an optimal control approach. Several different linearization methods were compared in [21]

giving rise to the analysis of artifacts in [6]. A numerical reconstruction method based on the Levenberg–Marquardt iteration was developed in [7, 34] and methods using an explicit least squares optimization approach are found in [1, 2, 33, 42]; the limited angle problem was considered in [23, 24]. See also, e.g. [28, 38, 39], for the case of anisotropic conductivities.

There is a lack of theoretical and computational studies addressing the full reconstruction procedure, i.e. first reconstructing the power density from boundary measurements from the acoustically perturbed current-to-voltage map, and then reconstructing the conductivity from the obtained power density. Mathematically, the (linearized) reconstruction of the power density is straightforward and consists of solving a Fredholm integral equation of the first kind, where the kernel is given by the pressure field. Assuming full control of the pressure field and noise-free measurement, this leads to a mildly ill-posed problem. When the pressure field is not fully controlled, the problem can become increasingly ill-posed. In [25] the problem with a not-fully known pressure field is investigated. However, we will see that this is a secondary concern and that the main problem of the first step is the signal-to-noise (SNR) ratio. It is questionable whether the measured signals are strong enough for reconstruction purposes, or if the measurements are completely altered by unavoidable barriers like the inevitable Johnson-Nyquist noise.

The aim of this paper is to conduct a computational study to clarify the feasibility of AET, using a simple model with realistic parameters. Even though the setup is idealized and neglects several important features of a real system, we believe such a computational study accommodated by mathematical analysis will give insight into the challenges of AET. The key parameter is the acousto-electric coupling constant, and we analyze the signal-to-noise ratio with respect to Johnson-Nyquist noise as a function of the coupling strength.

Our main finding is that the acousto-electric effect in human tissue is so weak that the measured signal is likely to be completely dominated by Johnson-Nyquist noise, and that even though the proposed inversion procedure performs well under severe noise conditions, it is not feasible to reconstruct the electrical conductivity in a medical imaging setting with AET.

The paper is organized as follows: In section 2 we discuss the modeling of the inverse problem, and explain the two-step inversion procedure and its numerical implementation. In section 3 the careful choice of physical parameters for the computational phantom is described, and the methods and tools for numerical simulation are introduced. Then in section 4 we derive a formula for the signal strength in terms of the relevant parameters, and compare this to an estimate of the Johnson-Nyquist noise, before describing the chosen noise model for the computational experiments. Numerical experiments are carried out in section 5 before conclusions are drawn in section 6.

2. Mathematical model and two step inversion procedure

In this section, we outline the governing mathematical model for the forward and inverse problem including the notation. We describe both in the continuous and discrete setting the procedure for the two-step inversion first taking the boundary measurements to the interior power densities, and next taking power densities to the conductivity.

2.1. Mathematical model

Assume that the object of interest occupies some bounded domain $\Omega \subset \mathbb{R}^d$, $d = 2, 3$, with smooth boundary $\partial\Omega$. The object Ω has the unknown isotropic electric conductivity $\sigma \in L^\infty_+(\Omega)$ (bounded from above and below by positive constants). Through electrodes attached

to the boundary, the normal current flux f is controlled, and consequently an interior electric potential u is generated. When no interior sources or sinks of charge are present inside Ω, the potential interior electric potential u is characterized by the generalized Laplace equation

$$\begin{cases} -\nabla\cdot(\sigma(x)\nabla u(x)) = 0, & x\in\Omega, \\ \sigma(x)\partial_\nu u(x) = f(x), & x\in\partial\Omega. \end{cases} \tag{2.1}$$

Here ν denotes the outward unit normal vector to the boundary $\partial\Omega$. We require that $f\in L^2_\diamond(\partial\Omega) = \{v\in L^2(\partial\Omega) : \int_{\partial\Omega} v\,\mathrm{d}s = 0\}$, i.e. the total input current vanishes. Then by classical theory for elliptic PDEs, (2.1) has a solution, and if we ground the potential by assuming $u|_{\partial\Omega}\in L^2_\diamond(\partial\Omega)$, then $u\in H^1(\Omega)$ is uniquely determined (see e.g. [16]). In EIT the aim is to reconstruct σ from several measurements of $g = u|_{\partial\Omega}$ corresponding to a set of different input currents f.

In AET the object is, in addition to the EIT measurement setup, penetrated by an acoustic wave that is generated by some source in the exterior of the domain, e.g. an ultrasound transducer. Let $p(x,t)$ denote the acoustic pressure at point x and time t generated by the source $S(x,t)$. We model the wave propagation by the scalar wave equation

$$\begin{cases} \left(\partial_t^2 - c^2(x)\Delta\right)p(x,t) = S(x,t), & (x,t)\in\mathbb{R}^d\times\mathbb{R}_+, \\ p(x,0) = \partial_t p(x,0) = 0, & x\in\mathbb{R}^d \end{cases} \tag{2.2}$$

equipped with suitable decay conditions. We consider the sound speed c and the source S to be known; then (2.2) is solvable and p is also known. When the acoustic wave travels through a material, the material is compressed and expanded. This results in a localized, time-dependent change in the electrical conductivity due to the so-called acousto-electric effect. We denote the acoustically perturbed conductivity by $\sigma_p(x,t)$. A reasonable, yet simple, model for σ_p is the following [4]:

$$\sigma_p(x,t) = \sigma(x)(1+\eta p(x,t)). \tag{2.3}$$

Here, $\eta > 0$ is the acousto-electric coupling parameter. We assume throughout that η is known and constant.

Figure 1 illustrates the acousto-electric effect. The source $S(x,t)$ is situated outside the disk-shaped domain Ω and generates an acoustic wave. As the wave propagates through the domain, the conductivity is perturbed; an instantaneous image of the perturbed conductivity is seen to the right.

The perturbation of σ gives rise to a perturbation of the electric potential. We denote by $u_p(x,t)$ this potential that for fixed $t\in\mathbb{R}_+$ solves the equation

$$\begin{cases} -\nabla\cdot(\sigma_p(x,t)\nabla u_p(x,t)) = 0, & x\in\Omega, \\ \sigma_p(x,t)\partial_\nu u_p(x,t) = f(x), & x\in\partial\Omega, \end{cases} \tag{2.4}$$

again with the convention $u_p|_{\partial\Omega}\in L^2_\diamond(\partial\Omega)$. The time-dependent perturbed electric measurement is now $g_p = u_p|_{\partial\Omega}$, for $t\in[0,T]$ for some sufficiently large acquisition time T.

In AET several boundary currents f and wave sources S are used, and the inverse problem is then to reconstruct the conductivity σ from measurements of the corresponding voltages $g(x), g_p(x,t)$, $x\in\partial\Omega$, $t\in[0,T]$.

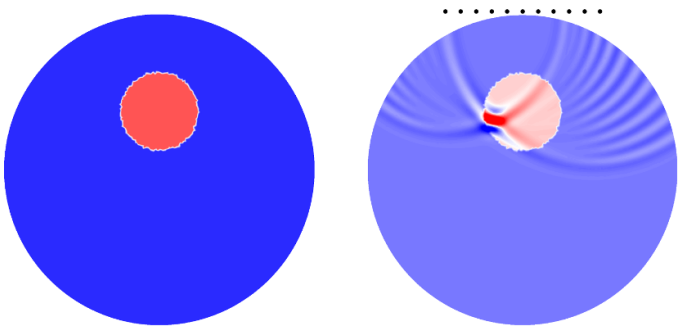

(a) Phantom (b) Acousto-electric effect

Figure 1. (a) Electric conductivity. (b) Perturbed conductivity due to the acousto-electric effect via a wave generated from transducers on the top; the effect is exaggerated for visibility.

2.2. Inversion step 1: from boundary measurements to power density

Multiplying (2.1) and (2.4) with u_p and u, respectively, subtracting, and integrating by parts yield the time series

$$\begin{aligned} I(t) &= \langle f, g_p - g \rangle_{L^2(\partial\Omega)} \\ &= \int_{\partial\Omega} f(x)\,(g_p(x,t) - g(x))\,\mathrm{d}S = -\eta \int_{\Omega} p(x,t)\,\sigma(x)\,\nabla u(x)\cdot\nabla u_p(x,t)\,\mathrm{d}x. \end{aligned} \tag{2.5}$$

Physically, $I(t)$ represents the change in the required total electric power for maintaining the current flux f at $\partial\Omega$ during the acoustic perturbation. Figure 2 illustrates how I behaves as an acoustic wave travels through an object. We will refer to $I(t)$ as the signal, and as the computation of $I(t)$ from the measurement is trivial, $I(t)$ will be the data from which we attempt to solve the inverse problem. Under the assumption that ηp is small, the approximation $u_p \approx u$ in $H^1(\Omega)$ is good (first order in η), and we obtain the linear approximation

$$I(t) \approx -\eta \int_{\Omega} p(x,t)\,\sigma|\nabla u(x)|^2\,\mathrm{d}x = -\eta \int_{\Omega} p(x,t)\,H(x)\,\mathrm{d}x. \tag{2.6}$$

The function $H(x) = \sigma|\nabla u(x)|^2$ is the interior power density. We will work in this linear regime.

By controlling the source S (see section 5 below) we generate a sequence of waves each with a different shape and focus in Ω. We represent all of these waves together by $p(x,t)$ concatenated sequentially in time. In the experiment, also the choice of boundary condition f in (2.1) is varied $f = f_i$, $i = 1,\ldots,N_f$. For each such condition there is a power density H_i related to the corresponding time signal I_i by

$$I_i(t) = -\eta \int_{\Omega} p(x,t)\,H_i(x)\,\mathrm{d}x, \quad 1 \leqslant i \leqslant N_f. \tag{2.7}$$

Using a finite element basis $\varphi_n(x)$, $n = 1,\ldots,N_\varphi$, we discretize in space and time, representing

$$H_i(x) = \sum_{n=1}^{N_\varphi} H_{i,n}\varphi_n(x), \quad \mathbf{H}_i = \left[H_{i,1},\ldots,H_{i,N_\varphi}\right]^T, \tag{2.8}$$

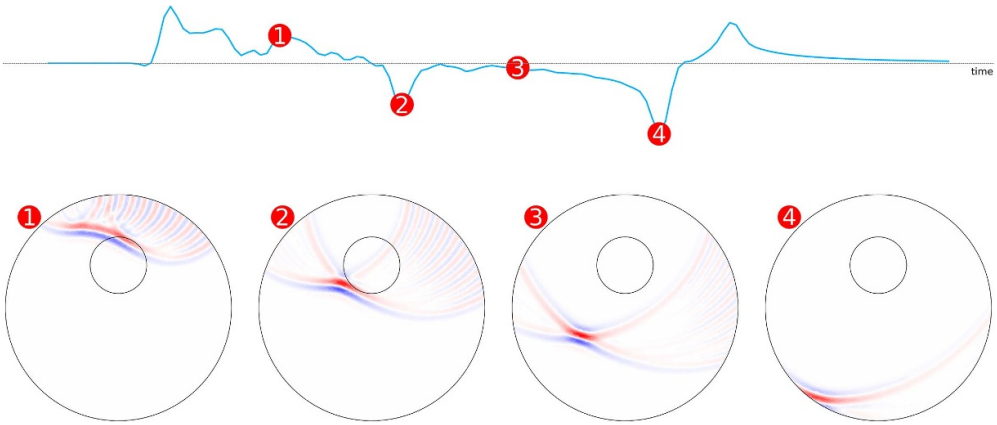

Figure 2. The top image contains the graph of the function $I(t)$ for the phantom seen in figure 1 corresponding to the illustrated propagating wave and the boundary condition $f(x,y) = x$. The red labels link the timestamps to their corresponding state of wave propagation visualized below the curve. The curve is a single wave from the numerical experiments in section 5—the details of the simulation approach are given in section 3.2.

$$p(x,t_j) = \sum_{n=1}^{N_\varphi} p_{j,n}\varphi_n(x), \tag{2.9}$$

$$\mathbf{I}_i = [I_i(t_1), \ldots, I_i(t_{N_t})]^T. \tag{2.10}$$

Let $\mathbf{M} = (a_{m,n})_{m,n}$ denote the mass matrix with elements $a_{m,n} = \int_\Omega \varphi_m\varphi_n \,\mathrm{d}x$ and $\mathbf{P} = (p_{j,m})_{m,j}$ the wave-matrix in which column j contains the finite elements coefficients of the wave at time t_j. Then we discretize the integral equation (2.6) by the matrix $\mathbf{K} = -\mathbf{P}^T\mathbf{M}$ acting on H

$$\eta\mathbf{K}\mathbf{H}_i = \mathbf{I}_i, \quad . \tag{2.11}$$

We then solve (2.11) by computing an SVD decomposition and regularize the solution by truncation.

2.3. *Inversion step 2: from power density to conductivity*

The problem of reconstructing σ from the interior power density data $\mathbf{H}$ has been explored in a variety of scenarios, see for example [5, 6, 17, 21, 30]. We approach this problem by minimizing the functional

$$\min_\sigma \mathcal{J}(\sigma) = \sum_{i=1}^{N_f} \|H_i(\sigma) - z_i\|_{L^1(\Omega)} + \beta|\sigma|_{\mathrm{TV}}, \tag{2.12}$$

where $z_i(x) = \sum_{n=1}^{N_\varphi} \mathbf{H}_{i,n}\varphi_n(x)$ is the reconstructed power density from step 1. The L^1 data-fidelity term is chosen to reflect the regularity of H: when σ has discontinuities, elliptic regularity theory only guarantees L^1-regularity of H; with $L^{1+\varepsilon}$-regularity for sufficiently small discontinuities, see [1].

For reconstruction we use the algorithm described in [1]. That is, we consider the following weighted quadratic problem arising from a linearization of (2.12),

$$J_{\sigma,\kappa'}(\kappa) = \frac{1}{2}\sum_{i=1}^{N_f}\int_\Omega w_i(\sigma,\kappa')\,|H_i'(\sigma)[\kappa] - z_{i,\sigma}|^2\,\mathrm{d}x + \frac{\beta}{2}\int_\Omega w_0(\sigma,\kappa')\,|\nabla(\sigma+\kappa)|^2\,\mathrm{d}x, \tag{2.13}$$

where $z_{i,\sigma} = z_i - H_i(\sigma)$ and the weights are

$$w_i(\sigma,\kappa') = |H_i'(\sigma)[\kappa'] - z_{i,\sigma}|_\epsilon^{-1}, \quad \text{for } 1 \leqslant i \leqslant N_f, \quad w_0(\sigma,\kappa') = |\nabla(\sigma+\kappa')|_\epsilon^{-1},$$

with $|\cdot|_\epsilon \equiv \sqrt{|\cdot|^2+\epsilon^2}$.

To solve (2.12) we initialize κ' as zero, compute the weights w_i, and successively do partial minimization of (2.13) to update κ' and thus the weights. After a few rounds of this, we update $\sigma := \sigma + \kappa'$ and restart the process. We do this following the steps outlined in [25] with the small modification that we in each step also project $\sigma := \sigma + \kappa$ to the interval $[10^{-2}, \infty)$ since σ cannot physically become negative or too close to 0, which would imply complete electrical isolation.

3. Parameters and numerical modeling

In this section, we describe the parameters and phantom used in the numerical experiments. Furthermore, we give a detailed description of the modeling and numerical simulation of the acoustic sources and fields, the electrical potential, and the measurements.

3.1. The computational phantom

We stick to a simple two-dimensional phantom for clarity and computational efficiency. The approach can in a straightforward way be generalized to more complex domains and structures in two and three dimensions. The computational phantom draws inspiration from breast cancer imaging: We assume a circular domain modeling a cross-section of the breast. The domain consists mostly of homogeneous material (in our case, normal breast tissue), and a small region where the conductivity differed (the cancerous tissue). The phantom is illustrated in figure 3(a).

For reference the domain $\Omega = \{x \in \mathbb{R}^2 : |x| < R\}$ with $R = 0.04\,\mathrm{m}$. The embedded region is also circular centered at $(0, 0.015)\,\mathrm{m}$ with radius $0.01\,\mathrm{m}$.

3.1.1. Electrical conductivity and boundary current density. Many authors have reported estimates of the electric conductivity in human tissue, and from [10, 20, 26] we infer that the electrical conductivity differs by a factor in the range 5–15 between healthy and cancerous breast tissue and experimental values for σ are reported to lie in the range 0.01–$1\,\mathrm{S\,m^{-1}}$, see, e.g. [8, 14, 20, 26]. In our experiments, we choose a high contrast conductivity phantom taking values in the range 0.1–$1.0\,\mathrm{S\,m^{-1}}$.

Further, the maximum allowed input current is $f_{\max} = 1\,\mathrm{mA}$ [14]. We enforce this by requiring that

$$\int_{\partial\Omega} f^+\,\mathrm{d}s \leqslant f_{\max}, \quad \text{where} \quad f^+(x) = \max\{f(x), 0\}.$$

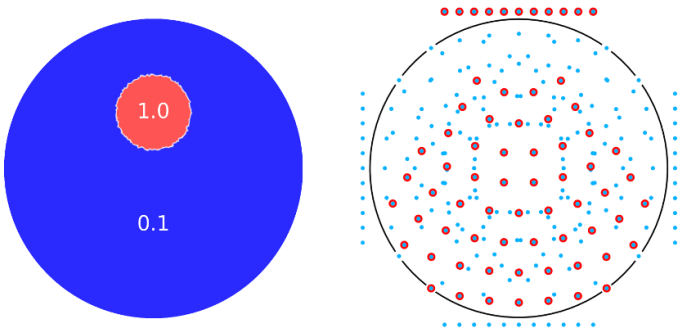

(a) Phantom (b) Focus points and transducers

Figure 3. (a) The phantom conductivity. The conductivity is 1.0 in the disc inclusion and the background is 0.1. (b) The points where the wavefronts get focused and the transducers. Each transducer focuses waves in a subset of the focus points. The red-ringed transducer at the top focuses in the cone of red-ringed points in the domain. The point distribution corresponding to each transducer is rotationally symmetric. In simulations, there are no gaps between transducer arrays and the domain.

3.1.2. Acousto-electric coupling and acoustic pressure. The value of the acousto-electric coupling constant η is of great importance. In [35], η in a rabbit heart is found to be approximately $0.041\,\mathrm{MPa}^{-1}$, i.e. $\eta \approx 4.1 \times 10^{-8}\,\mathrm{Pa}^{-1}$, while in [31, 32], values η in 0.9% NaCl solution is reported to be of the magnitude $10^{-9}\,\mathrm{Pa}^{-1}$. The value of η for breast tissue seems not to be known, but the mentioned values indicate a range of interest. We chose to perform our numerical experiments for $\eta = 10^{-8}$.

We choose the maximal amplitude of the acoustic pressure p to be $p_{\max} = 1.5\,\mathrm{MPa}$, in accordance with clinical standards [15], and assume a constant wave speed of $c_0 = 1500\,\mathrm{m\,s}^{-1}$ [15].

The acoustic wave is generated by a transducer array situated outside the phantom. The transducer array consists of equidistant individual point sources along a line segment. Each of the point sources excites one period of sine-wave with a frequency of 250 kHz. By controlling the time delay of the individual transducers, we can simulate many different wave patterns. We choose to work with focusing waves, i.e. waves that at a given time approximately concentrate at a certain point in the domain, see figures 1 and 2. We use 4 equidistant transducer positions around the boundary (above, below, left, right) and at each position, we have a unique set of 58 focus points as illustrated in figure 3(b): blue points indicate all focus points, red points the focus for the above positioning of the array. In table 1, we summarize our parameter choices.

Remark 3.1. We also tried a similar transducer setup but with plane waves, varying the frequencies and positions. This approach was less successful and resulted in poor reconstructions of the power density.

3.2. Simulation of the forward problem

3.2.1. Acoustic field and source terms. The expression (2.6) suggests that one could either choose a set of acoustic fields that approximate some basis (e.g. $L^2(\Omega)$), or a set of fields that approximate a Dirac delta distribution at a sufficiently large set of points in Ω. In this work, we have used different focused acoustic waves to sample the power density throughout the domain.

Table 1. Model parameters.

Parameter	Symbol	Value (s)	Unit
Conductivity	σ	0.1–1.0	S m^{-1}
Total boundary current flux	$f_{\max}$	1×10^{-3}	A
Acousto-electric coupling constant	η	10^{-8}	Pa^{-1}
Max. acoustic pressure	$p_{\max}$	1.5×10^{6}	Pa
Acoustic wave speed	c_0	1500	m s^{-1}
Domain radius	R	0.04	m

We simulate the acoustic field on a square finite difference grid containing Ω. K-WAVE is a MATLAB package that uses a k-space pseudo-spectral method to effectively and accurately solve the wave equation. For the source terms S_j of our acoustic field, we use a simplified transducer model. We model the action of the transducer as a linear array of $N_p = 11$ time-dependent volume point sources. We assign to the K-WAVE source function a discrete set of N_p grid points on a line segment of length $\ell = 4$ cm at the boundary of the domain; e.g. see figure 3(b). To suppress errors due to artificial wave reflections at the boundary of the computational domain, K-WAVE uses the so-called perfectly matched layers as a boundary condition.

Further, we use the focus functionality to delay the individual point source signals and orient the wave in various directions. See the K-WAVE function `focus.m` and the K-WAVE manual [44] for further details and explanations on this, and on how K-WAVE solves the wave equation.

We simulate acoustic fields with the above parameters on a uniform 350-by-350 grid with physical dimensions 12 cm $\times$ 12 cm. We place the transducer tangentially to the boundary at 4 equidistant points along the boundary. At each position, we focus the acoustic wave at a set of 58 points distributed in a cone originating at the transducer center. The 4 positions are illustrated in figure 3(b) where the cone of points corresponding to the top-most transducer location is also highlighted; we describe how this cone of points was chosen in the next section. We sample the waves equitemporally at $N_t = 141$ timestamps in the range 0 to T, where T is a uniform upper bound to let the wavefront propagate through the domain. T is set by K-WAVE. The acoustic fields $x \mapsto p(x, t_j)$ are then interpolated to the triangulated mesh for the domain Ω.

3.2.2. Focus point geometry. We construct the focus points by the following procedure: From the transducer location q we place a cone C with axis towards the center of Ω and angle θ between the axis and cone side. We choose a minimum distance $r_{\min}$ between focus points and the transducer and a focus point distance Δr.

Along each arc of the circle with center q and radius $r(k) = r_{\min} + k\Delta r$, $k = 1, \ldots,$ which has non-empty intersection with $C \cap \Omega$, we distribute the maximum number of points, with arc-distance Δr between them, symmetrically across the cone-axis.

For our simulations, illustrated in figure 3(b), we used the values

$$r_{\min} = \frac{R}{2}, \quad \Delta r = \frac{R}{5}, \quad \theta = \tan^{-1}\left(\frac{3}{4}\right).$$

3.2.3. Electric potential measurements. The electric potentials are computed by solving the PDE (2.1) using the open source computing framework FENICS [37].

The discretization is done using a $\mathcal{P}_1$ FEM-basis over a 16 617-node triangulated mesh for Ω. For each timestamp t_j and corresponding acoustic field $p(x, t_j)$ we compute the perturbed

conductivity $\sigma_p(x,t_j)$ according to (2.3). The PDE is then solved for the potential field $u_p(x,t_j)$ and we take the inner product of the difference between $u_p(x,t_j)$ and the static field $u(x)$ with the Neumann-boundary $f(x)$ on the boundary $\partial\Omega$ to obtain the derived data $I(t_j)$ as outlined by (2.5). Throughout we work with three different boundary conditions

$$f_1(x,y) = x, \quad f_2(x,y) = y, \quad \text{and} \quad f_3(x,y) = \frac{x+y}{\sqrt{2}}, \tag{3.1}$$

leading to the data $I_i(t_j)$ corresponding to f_i, each set bundled in vectors $\mathbf{I}_i$ as outlined in (2.10). It is known that two boundary conditions suffice [4] if cross measurements are also used; we compensate for such cross measurements by using the third boundary condition.

4. Signal and noise magnitude

We now investigate the consequences of the small acousto-electric effect. Independent of the precision of measurement devices and care taken to eliminate unwanted disturbances when conducting AET, there is a source of noise that cannot be eliminated; this is the so-called Johnson–Nyquist noise (also called thermal noise), and it is the noise due to the motion of the free electrons in the material itself. We refer to [18, 19] for more details regarding Johnson–Nyquist noise. If the voltage fluctuations caused by the random motion of free electrons are comparable (or greater) than those caused by the acoustic perturbation of the current-to-voltage map, the prospects for AET as a medical imaging technology are likely very limited.

As it is very complicated to accurately model such noise in a complex system like AET (the modeling must also involve the measurement equipment), we choose a different strategy. We instead derive a simple estimate for the AET signal magnitude $I(t)$ and the Johnson-Nyquist noise as a function of the central parameters. We then test our inversion method for various levels of noise (relative to $I(t)$). This then allows us to give a quantitative bound on the magnitude of the Johnson-Nyquist noise for which AET is feasible, given a specific set of parameters.

4.1. AET signal magnitude in a radial geometry

We now derive a simple estimate of the difference between an acoustically perturbed and unperturbed voltage signal. As before, let Ω be a disc in $\mathbb{R}^2$ of radius R and centered at the origin, and $\Omega_p = \{x \in \Omega : |x| < R_p \leqslant R\}$ be the part of Ω perturbed by the acoustic wave $p(x,t)$. Let $\sigma_0 > 0$ be a constant conductivity and let $\sigma_p = \sigma_0(1+\varepsilon\chi_{\Omega_p}(x))$, where $\chi_{\Omega_p}(x)$ is the characteristic function for Ω_p and $\varepsilon = \eta p_{\max}$ is small and dimensionless. For a boundary current $f \in L^2_\diamond(\partial\Omega)$, let u_0 be the solution of (2.1) for $\sigma := \sigma_0$, and u_p the solution of (2.4) with σ_p. As in (2.5) we form $I(t) = \langle f, g_p - g_0\rangle_{L^2(\partial\Omega)}$ where $g_p = u_p|_{\partial\Omega}$ and $g_0 = u_0|_{\partial\Omega}$.

We want to quantify $g_p - g_0$ and I in terms of the involved parameters, especially the coupling constant η. By separation of variables in polar coordinates, (see e.g. [40, pp 166–8]) we find that

$$g(\theta) = \sum_{n\in\mathbf{Z}} \frac{\hat{f}_n}{|n|\sigma_0} R e^{in\theta}, \quad g_p(\theta) = \sum_{n\in\mathbf{Z}} \frac{\hat{f}_n}{|n|\sigma_0} R e^{in\theta} \frac{2+\varepsilon\left(1-(R_p/R)^{2|n|}\right)}{2+\varepsilon\left(1+(R_p/R)^{2|n|}\right)}, \quad 0 \leqslant \theta < 2\pi,$$

where $\hat{f}_n$ is given by $\hat{f}_n = (2\pi)^{-1}\int_0^{2\pi} f(\theta)\mathrm{e}^{-in\theta}\mathrm{d}\theta$. We then get that

$$g_p(\theta) - g(\theta) = \sum_{n\in\mathbf{Z}} \frac{\hat{f}_n}{|n|\sigma_0} R\mathrm{e}^{in\theta}\left(-\frac{2\varepsilon\left(R_p/R\right)^{2|n|}}{2+\varepsilon\left(1+\left(R_p/R\right)^{2|n|}\right)}\right).$$

The function f is the current density of the input current. Setting $f = C_f\mathrm{e}^{i\theta}$ we obtain the requirement that

$$\int_{\partial\Omega} \max\left(\mathrm{Re}\left(f\right),0\right)\mathrm{d}\theta \leqslant f_{\max}, \tag{4.1}$$

which leads to $C_f = \frac{f_{\max}}{2R}$. Also, this choice for f yields

$$g_p(\theta) - g(\theta) = \frac{f_{\max}}{4\pi\,\sigma_0}\mathrm{e}^{i\theta}\left(-\frac{2\varepsilon\left(R_p/R\right)^2}{2+\varepsilon\left(1+\left(R_p/R\right)^2\right)}\right). \tag{4.2}$$

We define the boundary voltage amplitude A as the coefficient to $\mathrm{e}^{i\theta}$:

$$A = \frac{f_{\max}}{4\pi\,\sigma_0}\left(-\frac{2\varepsilon\left(R_p/R\right)^2}{2+\varepsilon\left(1+\left(R_p/R\right)^2\right)}\right).$$

For $\varepsilon \ll 1$ and using the boundary inner product formula for I (2.5) and the above choice for f and (4.1), we obtain

$$|A| \approx \frac{f_{\max}}{4\pi\,\sigma_0}\left(\varepsilon\left(R_p/R\right)^2\right) \quad \text{and} \quad |I| \approx \frac{f^2{}_{\max}R}{2\sigma_0}\left(\varepsilon\left(R_p/R\right)^2\right).$$

We use the parameters in table 1 and pick the perturbation radius as one-tenth of the domain radius $R_p = \frac{R}{10}$. Recall that $\varepsilon = \eta p_{\max}$. With these values, we find that

$$|A| \approx 1.2\times 10^{-7} \quad \text{and} \quad |I| \approx 3.0\times 10^{-11}.$$

The dependency of I on the parameters is interesting. Both $p_{\max}$ and η enters in ε and thus the magnitude $|I|$ linearly, whereas $f_{\max}$ enters quadratically. We can hence increase $|I|$ through $p_{\max}$ and $f_{\max}$, however these quantities are constrained by health considerations in particular in medical imaging applications.

4.2. Measurement noise and errors

As the above estimate shows that the signal magnitude is quite small, it is indeed warranted to consider the effect of Johnson–Nyquist noise in the SNR analysis. Usually, Johnson–Nyquist noise is modeled as a stochastic process independent of the other electrical activity going on. In a simple resistor system, it is an additive Gaussian white noise process, and the root-mean-square of the voltage signal of a thermal noise process is given by the formula

$$V_{\mathrm{RMS}} = \sqrt{4k_{\mathrm{B}}TR\,\Delta f}, \tag{4.3}$$

where $k_{\mathrm{B}} = 1.380649\times 10^{-23}$ is the Boltzmann constant, T the absolute temperature of the resistor, R the resistance and Δf the effective bandwidth of the measurement $g_p(t)$.

Although quantifying the thermal noise in a realistic AET scenario is immensely more complicated than for a resistor, we rely on the resistor model to get a rough estimate. For this, we need to assume some reasonable sizes for the involved quantities; we are mostly interested in the orders of magnitude rather than exact numbers. The temperature $T = 293.15\,\mathrm{K} \approx 20°\mathrm{C}$, that is living room temperature. The effective bandwidth is fixed to $\Delta f = 300\,\mathrm{kHz}$; the quantity can be estimated via the Fourier transform of the signal. Finally, the resistance R is in an EIT system in the range $1\,\mathbf{k\Omega}$–$100\,\mathbf{k\Omega}$. Plugging these numbers into (4.3) gives the estimate

$$V_{\mathrm{RMS}} = \sqrt{4k_{\mathrm{B}}TR\Delta f} \in (2.20\,\mu\mathrm{V}, 22.0\,\mu\mathrm{V})\,.$$

Let's for the moment fix $V_{\mathrm{JN}} = 10\ \mu\mathrm{V}$. The impact of the Johson–Nyquist noise on the I signal can then be estimated by

$$\begin{aligned} I_{\mathrm{JN}} &= \int_{\partial\Omega} V_{\mathrm{JN}}\, C_f \mathrm{d}\theta \\ &= \int_{\partial\Omega} V_{\mathrm{JN}} \frac{f_{\max}}{2R}\, \mathrm{d}\theta = \pi \cdot 10 \cdot 10^{-6} \cdot 10^{-3} = \pi\, 10^{-8}\,\mathrm{W}. \end{aligned}$$

Comparing the estimated Johnson–Nyquist noise $I_{\mathrm{JN}} = \pi \times 10^{-8}\,\mathrm{W}$ to the calculated signal $|I| \approx 3 \times 10^{-11}\,\mathrm{W}$ is quite discouraging. Even if these estimates are off by one or two orders of magnitude, it shows how the AET-signal is completely dominated by the Johnson–Nyquist noise. At best, one could by repeating the measurements improve the noise by one order of magnitude or two, and even possibly bring the signal and noise at par. We will in the next section numerically model the noise and work with an SNR of 0 dB and below; equivalently a relative noise level of 100% and more.

4.3. Noise modelling

In modeling the noise in AET there is a myriad of potential sources of stochasticity including, but not limited to, the exactness of the applied boundary current, the precision of boundary potential measurements, the knowledge of the wave (could be related to the precision of transducer positions, transducer timing, modeling limitations, wave speed, etc) and exactness of timestamps for measurements, etc.

We choose a simple and practical approach to noise modeling in line with what is usually done in inverse problems. We assume that the noise enters the model as additive Gaussian noise on the signal I.

Concretely, let $\mathbf{I}_i$ be the sampled true measurement of $I(t)$, see (2.10). We then add Gaussian noise by first generating the Gaussian vector $\mathbf{e} \sim \mathcal{N}(0, \mathbf{Id})$ and forming

$$\widetilde{\mathbf{I}}_i = \mathbf{I}_i + s\|\mathbf{I}_i\|_2 \left(\frac{\mathbf{e}}{\|\mathbf{e}\|_2} \right).$$

Here s indicates the relative noise level. In accordance with the analysis above, we will consider $s \in \{0, 1, 5, 10\}$, i.e. relative noise of $0\%, 100\%, 500\%$ and 1000%.

5. Numerical results and feasibility of AET

In this section, we put the theory and numerical methods to work on simulated measurements generated for the phantom in section 3. We first demonstrate that we can reconstruct the power density, and then apply our method to simulated measurements for a range of noise levels.

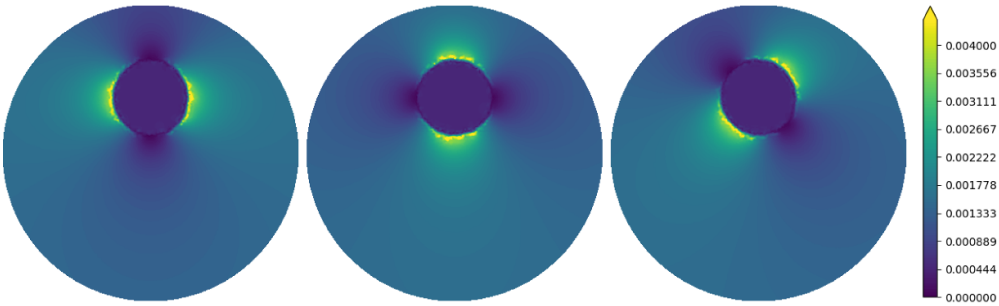

(a) $f_1(x,y) = x$ (b) $f_2(x,y) = y$ (c) $f_3(x,y) = \frac{1}{\sqrt{2}}(x+y)$

Figure 4. True power densities.

5.1. Step 1: reconstructing the power density

We pick the finite element basis φ_n, $n = 1,\ldots,N_\varphi$, from section 2 as a $\mathcal{P}_1$ basis on an unstructured 6065-node triangulated meshing for Ω. With this, we construct the discretized integral operator from equation (2.11) with the discretized waves $p(x,t)$ temporally sampled in the timestamps corresponding to the timestamps of the given noisy data $\widetilde{\mathbf{I}}_i$.

We solve the equation (2.11) for $\mathbf{H}_i$ using a truncated singular value decomposition, though not straightforward from $\mathbf{K}$. Instead, we rewrite the equation on the form

$$\widetilde{\mathbf{K}}\widetilde{\mathbf{H}}_i = \widetilde{\mathbf{I}}_i \tag{5.1}$$

where $\widetilde{\mathbf{K}} = \eta\mathbf{K}\mathbf{L}^{-T}$, $\widetilde{\mathbf{H}}_i = \mathbf{L}^T\mathbf{H}_i$ and $\mathbf{L}$ is the Cholesky factor of the mass matrix $\mathbf{M} = \mathbf{L}\mathbf{L}^T$.

We then take a singular value decomposition $(\mathbf{U},\mathbf{\Sigma},\mathbf{V}^T)$ of $\widetilde{\mathbf{K}}$ and do a truncated reconstruction of $\widetilde{\mathbf{H}}_i$. To this end we construct the truncated pseudo-inverse $\mathbf{\Sigma}_k^\dagger$ and compute

$$\widetilde{\mathbf{H}}_i = \mathbf{V}\mathbf{\Sigma}_k^\dagger\mathbf{U}^T\widetilde{\mathbf{I}}_i,$$

where k is the truncation threshold. We can then recover $\mathbf{H}_i$ from that result by inverting $\mathbf{L}^T$.

This is done for each $\mathbf{H}_i$ corresponding to each of the boundary conditions in (3.1).

Remark 5.1. The reason for this restructuring of (2.11) before the singular value decomposition is that the resulting decomposition corresponds to a decomposition for the wave matrix $\mathbf{P}^T$ such that if we take the matrix $\widetilde{\mathbf{V}} = \mathbf{L}^{-T}\mathbf{V}$ then it is the right singular vectors for $\mathbf{P}^T$ in a space where the inner product is $\langle\cdot,\cdot\rangle_{\mathbf{M}}$, that is in the discretized $L^2(\Omega)$ inner product; so $\widetilde{\mathbf{V}}^T\mathbf{M}\widetilde{\mathbf{V}} = \mathbf{Id}$. Hence the singular vectors of $\widetilde{\mathbf{V}}$ have a meaningful visualization on our finite element mesh.

In figure 4 we illustrate the true power densities H_i computed by solving the forward problem for the boundary conditions f_i. These compare to figure 5 containing power density reconstructions from data with varying levels of relative noise.

Different levels of truncation of the singular values have been used in the reconstruction in order to regularize the inversion method. These power densities are later used in the reconstruction of the conductivities. The three power density reconstructions in each row are what goes into the reconstruction of the conductivity.

The truncation level was chosen by running the full reconstructions of the conductivity for a limited range of choices and picking what seemed to be the best options. The search was not exhaustive.

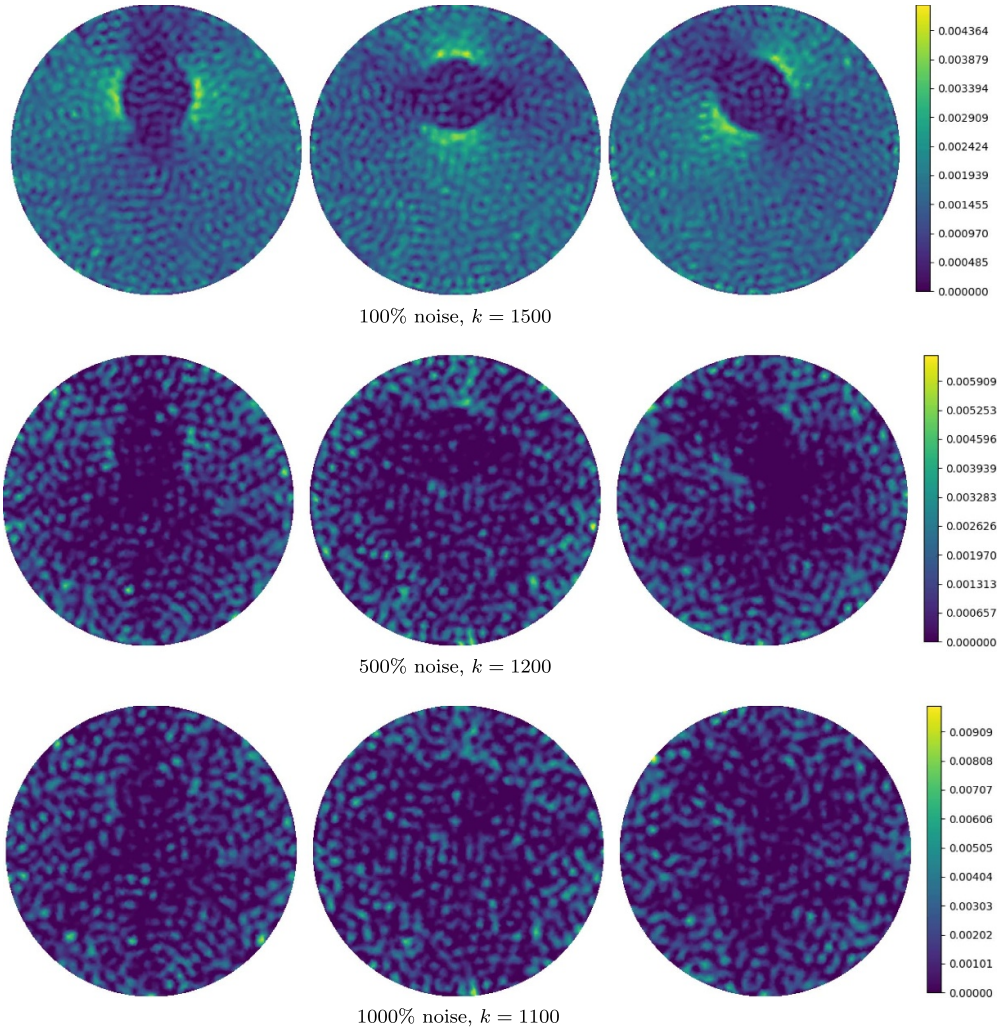

Figure 5. Reconstruction of the power densities H_i from data with an added relative noise. k is the number of singular values used in the TSVD reconstruction for H. We denote in each row the used truncation k as well as the level of relative noise. Each column i corresponds to boundary condition f_i.

We would like to draw attention to the most significant features in figure 5, the peaks enclosing the location of the inclusion. These are more or less defining for the ability to reconstruct the conductivity. In the whole domain there are a lot of errors reminiscent of something like the interference pattern of waves. While they introduce some errors in the conductivity reconstruction, they do not form singularities that may produce wrong inclusions in the final conductivity.

We remark that the colorbars are not the same for all the power density reconstructions. The scale of the oscillations of the errors drown out more delicate features, but as we see later for the reconstructions of the conductivities some of the important parts must remain.

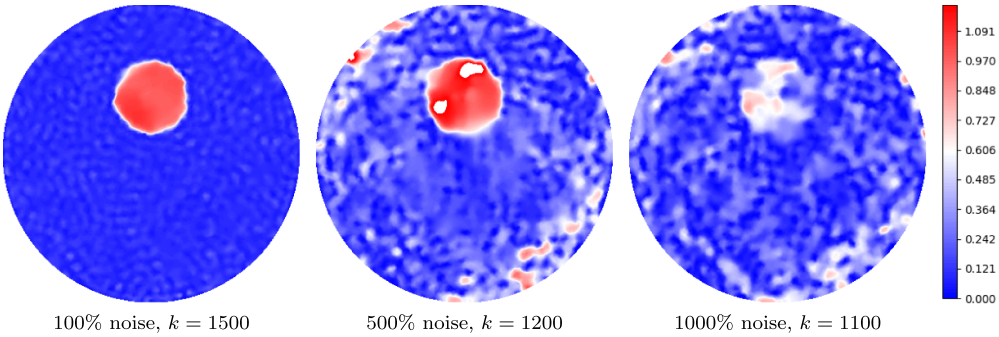

Figure 6. Reconstruction of the conductivity from data with an added relative noise. k is the number of singular values used in the TSVD reconstruction for H.

5.2. Step 2: reconstructing the electrical conductivity

We reconstruct the conductivity using the approach outlined in section 2 following, as mentioned there, the steps taken in [1, 25].

The reconstructions corresponding to varying levels of relative noise are shown in figure 6. As mentioned in the former section, they were each reconstructed from the corresponding row-sets of power densities illustrated in figure 5. We see here how robust to noise the reconstruction is, with us being able to discern the inclusion even at incredibly high levels of noise.

We ascribe this largely to the level of redundancy in the data from the multiple waves used to perturb the domain. Also likely, the robustness of the model to random noise possibly exiting the model's range plays a part here. This latter aspect was also observed in [25] for defects from reconstruction using an erroneous wave. The largely erroneous features in the power density background were shown to have limited impact on the final reconstruction of the conductivity because they lacked coherence across the multiple power densities going into the reconstruction.

While we do observe the reconstruction quality suffers from the heavy increase in noise levels, the inclusion remains somewhat observable even at the highest level of noise.

6. Conclusions, discussion and further work

In this manuscript, we have studied the feasibility of AET. The motivation is to better understand to what extent AET can provide a modality for stable imaging of the electrical conductivity in realistic and relevant situations. Our computational phantom therefore builds from parameters motivated by medical imaging.

We have suggested a mathematical and computational model for the complete inversion framework for AET and tested it on synthetic data for different values of noise. Moreover, we have analyzed the signal magnitude, a critical element in AET. There are many parameters affecting this quantity, including the pressure of ultrasound waves and the electrical conductivity of the body. Not surprisingly, the most important factor is the strength of the acousto-electric coupling; since the acoustic-electric coupling is very weak, both simulations and our estimates show that the AET signal is very weak.

We have further investigated the critical and unavoidable Johnson–Nyquist noise. Due to the small amplitude signal of AET, this low amplitude background noise needs to be accounted for, regardless of the quality of the equipment and other forms of measurement noise; it can

only really be dealt with by data redundancy, re-sampling, and model robustness. The precise magnitude of the Johnson–Nyquist noise is highly system-dependent, but we have attempted a qualified guess on the order of magnitude. Our estimate of the Johnson–Nyquist noise is several orders of magnitude larger than the signal; this makes imaging tremendously difficult.

Despite the challenging conditions, we have tested our inversion method on simulated data that are highly perturbed by noise. The results indicate that with an SNR of 0 dB (relative error of 100%) we achieve surprisingly good reconstructions, and even with an SNR of −10 dB (relative error of 1000%), some features remain.

The relatively good performance in these hostile noise conditions indicates that mathematically the AET reconstruction problem is fairly well-posed, and the data contain lots of redundant information stemming from the choice of acoustic waves, the sampling of I, and the number of electric boundary conditions.

Our final assessment of AET is that it is unlikely to be feasible for high-resolution medical imaging without a large improvement of the SNR. Such an improvement can only be achieved by a very large number of repeated experiments. This is at least the case in medical imaging, where signal strength is (wisely) curbed by multiple health considerations. It might, however, be possible for AET to obtain some additional and useful information for diagnostic purposes, or for non-destructive testing in materials science, where one is allowed to use higher pressure and current.

Clearly, our modeling suffers from many simplifications, but going to more realistic electrode modeling, more complex geometries in 3D, and other realistic wave models is certainly possible using a similar approach; we leave such interesting projects for future studies. A more detailed modeling of the Johnson–Nyquist noise in AET is very relevant. This depends most likely on various system settings and makes most sense when a particular system is projected and built.

Data availability statement

The data that support the findings of this study are available upon request from the authors.

Acknowledgments

Parts of this work was done while Bjørn Jensen and Adrian Kirkeby were at DTU. The project was supported by the Villum Foundation (Grant No. 25893).

ORCID iDs

Bjørn Jensen https://orcid.org/0000-0002-4743-2631
Adrian Kirkeby https://orcid.org/0000-0003-2741-7423
Kim Knudsen https://orcid.org/0000-0002-4875-3074

References

[1] Adesokan B J, Jensen B, Jin B and Knudsen K 2019 Acousto-electric tomography with total variation regularization *Inverse Problems* **35** 035008
[2] Adesokan B J, Knudsen K, Krishnan V P and Roy S 2018 A fully non-linear optimization approach to acousto-electric tomography *Inverse Problems* **34** 104004
[3] Adler A and Holder D 2021 *Electrical Impedance Tomography: Methods, History and Applications* (CRC Press)

[4] Alberti G S and Capdeboscq Y 2018 *Lectures on Elliptic Methods for Hybrid Inverse Problems* vol 25 (Société Mathématique de France)

[5] Ammari H, Bonnetier E, Capdeboscq Y, Tanter M and Fink M 2008 Electrical impedance tomography by elastic deformation *SIAM J. Appl. Math.* **68** 1557–73

[6] Bal G, Hoffmann K and Knudsen K 2018 Propagation of singularities for linearised hybrid data impedance tomography *Inverse Problems* **34** 024001

[7] Bal G, Naetar W, Scherzer O and Schotland J 2013 The Levenberg-Marquardt iteration for numerical inversion of the power density operator *J. Inverse Ill-Posed Problems* **21** 265–80

[8] Barber D C and Brown B H 1984 Applied potential tomography *J. Phys. E: Sci. Instrum.* **17** 723

[9] Berthon B, Behaghel A, Mateo P, Dansette P-M, Favre H, Ialy-Radio N, Tanter M, Pernot M and Provost J 2019 Mapping biological current densities with ultrafast acoustoelectric imaging: application to the beating rat heart *IEEE Trans. Med. Imaging* **38** 1852–7

[10] Bidhendi H K, Jafari H M and Genov R 2014 Ultra-wideband imaging systems for breast cancer detection *Ultra-Wideband and 60 GHz Communications for Biomedical Applications* (Springer) pp 83–103

[11] Calderón A-P 1980 On an inverse boundary value problem *Seminar on Numerical Analysis and Its Applications to Continuum Physics (Rio de Janeiro, 1980)* (Sociedade Brasileira de Matemática) pp 65–73

[12] Capdeboscq Y, Fehrenbach J, de Gournay F and Kavian O 2009 Imaging by modification: numerical reconstruction of local conductivities from corresponding power density measurements *SIAM J. Imaging Sci.* **2** 1003–30

[13] Cheney M, Isaacson D and Newell J C 1999 Electrical impedance tomography *SIAM Rev.* **41** 85–101

[14] Cherepenin V, Karpov A, Korjenevsky A, Kornienko V, Mazaletskaya A, Mazourov D and Meister D 2001 A 3D electrical impedance tomography (EIT) system for breast cancer detection *Physiol. Meas.* **22** 9

[15] Demi M 2014 2.12—the basics of ultrasound *Comprehensive Biomedical Physics* ed A Brahme (Elsevier) pp 297–322

[16] Evans L C 2022 *Partial Differential Equations* vol 19 (American Mathematical Society)

[17] Gebauer B and Scherzer O 2008 Impedance-acoustic tomography *SIAM J. Appl. Math.* **69** 565–76

[18] Gillespie D T 1996 The mathematics of Brownian motion and Johnson noise *Am. J. Phys.* **64** 225–40

[19] Gillespie D T 1998 Theory of electrical noise induced in a wire loop by the thermal motions of ions in solution *J. Appl. Phys.* **83** 3118–28

[20] Hesabgar S M, Sadeghi-Naini A, Czarnota G and Samani A 2017 Dielectric properties of the normal and malignant breast tissues in xenograft mice at low frequencies (100 Hz–1 MHz) *Measurement* **105** 56–65

[21] Hoffmann K and Knudsen K 2014 Iterative reconstruction methods for hybrid inverse problems in impedance tomography *Sens. Imaging* **15** 96

[22] Holder D S 2010 *Electrical Impedance Tomography: Methods History and Applications* (*Series in Medical Physics and Biomedical Engineering*) (IOP Press)

[23] Hubmer S, Knudsen K, Li C and Sherina E 2018 Limited-angle acousto-electrical tomography *Inverse Problems Sci. Eng.* **27** 1–20

[24] Jensen B, Knudsen K and Schlüter H 2023 Conductivity reconstruction from power density data in limited view *Math. Scand.* **129** 140–60

[25] Jensen B C S and Knudsen K 2021 Sound speed uncertainty in acousto-electric tomography *Inverse Problems* **37** 125011

[26] Joines W T, Zhang Y, Li C and Jirtle R L 1994 The measured electrical properties of normal and malignant human tissues from 50 to 900 MHz *Med. Phys.* **21** 547–50

[27] Karhunen K, Seppänen A, Lehikoinen A, Monteiro P J M and Kaipio J P 2010 Electrical resistance tomography imaging of concrete *Cem. Concr. Res.* **40** 137–45

[28] Knudsen K, Markvorsen S and Schlüter H 2023 Reconstructing anisotropic conductivities on two-dimensional Riemannian manifolds from power densities (arXiv:2202.12056 [math.AP])

[29] Kuchment P and Kunyansky L 2010 Synthetic focusing in ultrasound modulated tomography *Inverse Problems Imaging* **4** 665–73

[30] Kuchment P and Kunyansky L 2011 2D and 3D reconstructions in acousto-electric tomography *Inverse Problems* **27** 055013

[31] Lavandier B, Jossinet J and Cathignol D 2000 Experimental measurement of the acousto-electric interaction signal in saline solution *Ultrasonics* **38** 929–36
[32] Lavandier B, Jossinet J and Cathignol D 2000 Quantitative assessment of ultrasound-induced resistance change in saline solution *Med. Biol. Eng. Comput.* **38** 150–5
[33] Li C, An K, Zheng K and Lesselier D 2020 A complete framework for acousto-electric tomography with numerical examples *IEEE Access* **8** 9091858
[34] Li C, Karamehmedovic M, Sherina E and Knudsen K 2021 Levenberg-Marquardt algorithm for acousto-electric tomography based on the complete electrode model *J. Math. Imaging Vis.* **63** 492–502
[35] Li Q, Olafsson R, Ingram P, Wang Z and Witte R 2012 Measuring the acoustoelectric interaction constant using ultrasound current source density imaging *Phys. Med. Biol.* **57** 5929
[36] Liu D, Khambampati A K, Kim S and Kim K Y 2015 Multi-phase flow monitoring with electrical impedance tomography using level set based method *Nucl. Eng. Des.* **289** 108–16
[37] Logg A, Mardal K-A and Wells G 2012 *Automated Solution of Differential Equations by the Finite Element Method: The FEniCS Book* vol 84 (Springer)
[38] Monard F and Bal G 2012 Inverse anisotropic diffusion from power density measurements in two dimensions *Inverse Problems* **28** 084001
[39] Monard F and Rim D 2018 Imaging of isotropic and anisotropic conductivities from power densities in three dimensions *Inverse Problems* **34** 075005
[40] Mueller J L and Siltanen S 2012 *Linear and Nonlinear Inverse Problems With Practical Applications* vol 10 (SIAM)
[41] Olafsson R, Witte R, Jia C, Huang S-W, Kim K and O'Donnell M 2009 Cardiac activation mapping using ultrasound current source density imaging (UCSDI) *IEEE Trans. Ultrason. Ferroelectr. Freq. Control* **56** 4816064
[42] Roy S and Borzì A 2018 A new optimization approach to sparse reconstruction of log-conductivity in acousto-electric tomography *SIAM J. Imaging Sci.* **11** 1759–84
[43] Saturnino G B, Madsen K H and Thielscher A 2019 Electric field simulations for transcranial brain stimulation using FEM: an efficient implementation and error analysis *J. Neural Eng.* **16** 066032
[44] Treeby B E and Cox B T 2010 k-Wave: MATLAB toolbox for the simulation and reconstruction of photoacoustic wave fields *J. Biomed. Opt.* **15** 021314
[45] Widlak T and Scherzer O 2012 Hybrid tomography for conductivity imaging *Inverse Problems* **28** 084008
[46] Zhang H and Wang L V 2004 Acousto-electric tomography *Proc. SPIE* **5** 20